AIAA SciTech Forum
January 3-7, 2022, San Diego, CA & Virtual
AIAA SCITECH 2022 Forum

10.2514/6.2022-0649

Micromechanics modeling of time-dependent failure of stowed high-strain composite structures

Uba K Ubamanyu* and Sergio Pellegrino†
California Institute of Technology, Pasadena, CA, 91125, USA.

Deployable structures made of thin-ply carbon fiber-reinforced composites are of interest due to their high stiffness to weight ratio, high packaging efficiency, and ability to deploy by the release of stored strain energy. For most applications, the largest strains are applied for the longest time during stowage, and viscoelastic polymers in these fiber-reinforced composites are prone to time-dependent deformation growth and rupture. This paper presents a study of the time-dependent deformation growth and time-dependent failure mechanisms using a micromechanics-based 3D finite element model representation of the composite. The study is focused on a repeating unit cell of a cross-ply carbon fiber laminate consisting of linear-elastic transversely isotropic fibers embedded in a linear viscoelastic matrix. A parametric study of initial fiber misalignment angle and its influence on the deformation growth and time to rupture is presented.

I. Introduction

Time-dependent behavior of polymers manifests itself in various ways, such as creep under constant load, stress relaxation under constant deformation, time-dependent recovery of deformation after removal of load, and time-dependent creep/relaxation rupture [1]. These behaviors are also relevant to fiber-reinforced composites, as these engineered materials consist of fibers embedded in a polymeric matrix. The ability to self-deploy using stored strain energy draws attention towards fiber-reinforced composites as an efficient material for large spacecraft. High strain composite is made of ultra-thin prepregs that exhibits more strength and stiffness per unit mass than most metallic materials. High strain composite that undergoes large deformation and curvature can be tightly coiled around a central hub to achieve high packing efficiency. High strain deployable structures [2] are of increasing interest due to their high stiffness to weight ratio, high packaging efficiency, and ability to deploy by the release of stored strain energy.

Deployable structures undergo various loading states during their lifetime. For a typical high strain deployable structure, the largest strains are applied for the longest time during its stowage for launch. The presence of a viscoelastic polymer may result in excessive time-dependent deformation growth and rupture during extended stowage periods and hence, understanding the time-dependent behavior of these composites during stowage is essential.

Stress relaxation in response to the curvature imposed during stowage significantly affects both the deployment process and the deployed performance of the structure [3, 4]. If the stowage period is sufficiently long, cracks have been observed on the compression surface [5, 6]. Extensive research was previously carried out on the failure of fiber-reinforced composites due to fiber microbuckling and kink band formation under axial compression [7, 8]. Recent research has studied the effect of stowage on the deployment behavior, both experimentally and numerically [9–11]. Initial investigations of rupture due to stress relaxation of composite coupons were performed using the Flattening to Rupture (FTR) test. Observations using μCT imaging showed that the rupture occurs near the compression surface and involves kink-band formation, fiber-matrix debonding, and inter-lamina delamination [5]. However, the interaction of microstructural failure mechanisms causing rupture under long-duration curvature has not been studied. It has been hypothesized that the stress relaxation of the matrix aids the microstructural deformation growth and eventually triggers the rupture through fiber microbuckling and/or fiber-matrix debonding mechanisms.

Here we present a study of the time-dependent deformation growth and failure mechanisms using a micromechanics-based 3D finite element model representation of a composite laminate. Fiber microbuckling and fiber-matrix debonding mechanisms are considered in a parametric study to understand and validate a hypothesized sequence of failure events. Our current study is focused on cross-ply carbon fiber laminate made of IM7 carbon fibers and PMT-F7G epoxy matrix

*Graduate Student, Graduate Aerospace Laboratories, 1200 E California Blvd, MC 105-50, Pasadena.AIAA Student Member. Email: ubamanyu@caltech.edu

†Joyce and Kent Kresa Professor of Aerospace and Civil Engineering, Graduate Aerospace Laboratories, 1200 E California Blvd, MC 105-50, Pasadena. AIAA Fellow. E-mail: sergiop@caltech.edu

modeled as linear elastic transversely isotropic fibers embedded in a linear viscoelastic matrix. Section II explains the details of the micromechanics-based finite element model and the material models. Using this model, Section III presents the microstructural deformation growth over time and rupture due to fiber microbuckling. Section IV, presents a parametric study of the initial misalignment angle. Section V, concludes the paper and outlines further work currently in progress.

II. Details of micromechanics model

A. Representative volume element (RVE)

A micromechanical finite element model of a bending test was developed in the commercial finite element software Abaqus/Standard with the goal of studying the time-dependent deformation growth of the microstructure and failure mechanisms such as fiber microbuckling and fiber-matrix interface debonding. To achieve computational efficiency, a repeating representative volume element of a carbon fiber reinforced polymer matrix cross-ply (0/90/0) laminate with periodic boundary conditions was modeled. To model bending problems, the RVE must include the entire thickness of the laminate.

The RVE consists of hexagonally packed fibers with an initial misalignment described below and the fiber-matrix interfaces were modeled as cohesive surfaces for the 0° ply on the compression side. The other two plies (90 and 0 plies) were modeled as homogenized orthotropic solids to reduce the size of the computational model. This decision was supported by the experimental observation that the rupture only occurs near the compression surface while the plies on the tension side remain intact [5].

The model has a length of 500 μm in the longitudinal fiber direction and a thickness of 162 μm. A nominal fiber volume fraction of 50% and the fiber diameter of 5.2 μm was considered. The width of the RVE was chosen equal to the fiber spacing. The fiber spacing, c, was calculated from,

$$c = d\sqrt{\frac{\pi\sqrt{3}}{6V_f}} = 7\mu m \tag{1}$$

where d is the fiber diameter, and V_f is the fiber volume fraction, assuming hexagonal packing of the fibers.

An initial fiber misalignment was defined using the arctan function with a slope, $\phi_0 = 1^\circ$ at the center and an amplitude, λt, where λ is assumed to be 0.05 and t is the ply thickness. The longitudinal profile of a fiber with this initial misalignment is shown in Fig. 1.

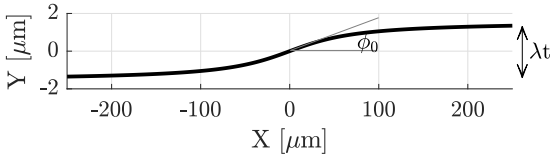

Fig. 1 Longitudinal profile of a fiber with initial misalignment.

A schematic of a 3D cross-ply composite laminate subjected to uniform bending along with the boundary conditions prescribed and the cross-sectional view are shown in Fig. 2. The green and blue regions represent the fibers and matrix, respectively. The red region corresponds to the homogenized 90 and 0-degree laminae.

The X-axis is defined in the direction of the fibers in the 0° ply and the Y-axis is defined perpendicular to the mid-plane of the laminate. The boundary condition on the faces of RVE must ensure periodic behavior in the Z-direction. Hence, periodic conditions were applied directly to corresponding nodes using the $*Equation$ constraint in Abaqus, which requires the mesh to be identical on those faces. The X and Y components of the displacement (u and v, respectively) of each node on one face were set equal to their corresponding node on the opposite face:

$$u(x, y, 0) = u(x, y, c) \tag{2}$$

$$v(x, y, 0) = v(x, y, c) \tag{3}$$

The difference between the displacement in the Z-direction, w, of corresponding nodes was forced to be uniform over the RVE in order to constrain the change in width of the RVE:

$$w(x_i, y_i, 0) - w(x_i, y_i, c) = \text{constant for all node pairs} \tag{4}$$

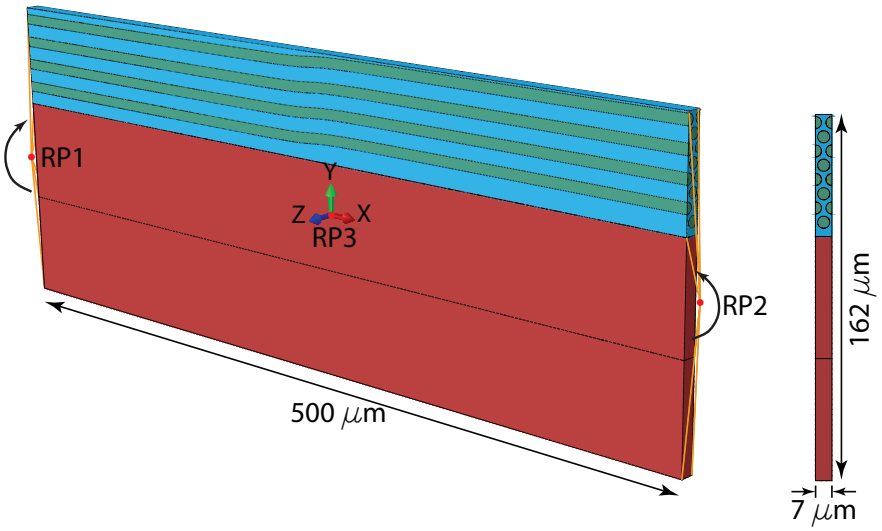

Fig. 2 Micromechanics-based finite element model of RVE.

In terms of the length of the RVE, a central 0.5 mm long section was simulated to reduce the computational cost. The end cross-sections of the RVE were constrained to remain co-planar while the relative position of the plane was left unconstrained. All the nodes at the end cross-section were coupled to a reference point (one for each face). To ensure equal end moment loading, the rotational degrees of freedom of reference points RP1 and RP2 were constrained to reference point RP3 by prescribing the condition given in Eq.(5), using the $*Equation$ constraint in Abaqus;

$$\theta_Z^{RP1} - \theta_Z^{RP2} = \theta_Z^{RP3} \tag{5}$$

where θ_Z is the rotation about the global Z-axis.

Loading was applied by increasing θ_Z^{RP3} from 0 to a specific magnitude θ at the reference point RP3 during a static step in which the response is time-independent, followed by holding the rotation θ, for $1{\times}10^{10}$ s during a time-dependent visco step. Translations in all directions were constrained at one reference point, while the other reference point was left unconstrained along the X-axis, in order to allow length changes while avoiding any rigid body motions. The model consisted of 8-node brick elements (C3D8R) with a characteristic mesh size of 1 μm. A static loading step followed by a viscoelastic step with non-linear geometry was used in all of the analyses presented here.

B. Material model

The fibers were assumed linear-elastic and transversely isotropic. Time-dependent effects in the fiber are order of magnitudes smaller than in the matrix [12] and hence, the fibers are assumed to be time-independent. The properties of the IM7 carbon fibers are given in Table 1, taken from [13].

Table 1 Properties of IM7 fibers

Parameter	Value
Fiber diameter	5.2 μm
Axial modulus E_{f1}	276 GPa
Transverse modulus $E_{f2} = E_{f3}$	13.8 GPa
Axial shear modulus $G_{f12} = G_{f13}$	9.5 GPa
Transverse shear modulus G_{f23}	5.52 GPa
Longitudinal Poisson's ratio $\nu_{f12} = \nu_{f13}$	0.22
Transverse Poisson's ratio ν_{f23}	0.25

The polymer matrix was modeled as an isotropic, linear viscoelastic solid defined by a Prony series at 70 °C. The Prony series representation of the relaxation modulus is given by,

$$E(t) = E_\infty + \sum_{i=1}^{n} E_i e^{-(t/\tau_i)} \tag{6}$$

where t is time, E_∞ is the long term modulus, E_i are the Prony coefficients and τ_i are the relaxation times. Each exponential term corresponds to the variation of the relaxation modulus over a time period. The number of terms included in the Prony series depends on the time scale of the problem of interest. The Prony series used for the analysis, measured experimentally using PMT-F7G neat resin samples, is given in Table 2. A constant Poisson's ratio of 0.33 was assumed.

Table 2 Relaxation times and Prony coefficients for PMT-F7G epoxy at 70 °C

i	E_i, MPa	τ_i, s
∞	1716.5	-
1	95.1	1.470 e-3
2	137.3	7.351 e-3
3	138.4	7.351 e-2
4	157.9	7.351 e-1
5	142.7	7.351 e+0
6	129.2	7.351 e+1
7	88.5	7.351 e+2
8	87.4	7.351 e+3
9	83.2	7.351 e+4
10	71.3	7.351 e+5
11	117.9	7.351 e+6
12	30.6	7.351 e+7

The homogenized material properties of the unidirectional lamina made of IM7 carbon fiber and PMT-F7G are given in Table 3, taken from [14]. Since our focus is to study the time-dependent deformation growth at the microstructural scale and the homogenized part of the model represent material regions that are loaded under tension and/or low compression, to reduce the scale of the numerical simulations the homogenized regions are assumed to be time-independent.

Table 3 Properties of IM7/PMT-F7G lamina

Parameter	Value
Lamina thickness	54 μm
Axial modulus E_1	122.2 GPa
Transverse modulus $E_2 = E_3$	6.5 GPa
Axial shear modulus $G_{12} = G_{13}$	4.753 GPa
Transverse shear modulus G_{23}	3.898 GPa
Longitudinal Poisson's ratio $\nu_{12} = \nu_{13}$	0.27
Transverse Poisson's ratio ν_{23}	0.27

A cohesive surface contact model was defined for the fiber-matrix interface, to allow debonding to occur. The contact formulation models debonding through an effective traction-separation law that assumes initially linear elastic behavior followed by the initiation and evolution of damage [15]. It is defined by the cohesive strengths, σ_c or τ_c, and

the fracture toughness, G_c, in each fracture mode (mode I, mode II, and mode III). The maximum stress criterion was assumed, for the damage to initiate when the maximum contact stress ratio reaches the value one. The damage evolution was defined based on the fracture energy using a power-law mixed-mode fracture criterion. The cohesive damage properties used for the fiber-matrix interface are listed in Table 4, taken from [16].

Table 4 Cohesive damage properties

σ_c (N/mm^2)	G_{Ic} (kJ/m^2)	$\tau_{2c} = \tau_{3c}$ (N/mm^2)	$G_{IIc} = G_{IIIc}$ (kJ/m^2)
23.0	0.139	88.0	0.445

III. Analysis and observations

This section presents the analysis carried out using the micromechanics model described in Section II. A mesh of 8-node brick elements with enhanced hourglassing control with characteristic length of 1 μm was found to produce a converged moment-curvature response with a reasonable computational time through the mesh sensitivity analysis. Characteristic lengths of 0.5 μm, 0.75 μm, 1.0 μm, and 1.25 μm were considered during this mesh sensitivity analysis. All the analysis presented in this section and Section IV consist of the mesh with a characteristic length of 1 μm.

A typical moment-curvature response for the micromechanics model with initial misalignment angle $\phi_0 = 1^\circ$ is shown in Fig. 3. Uniform bending was applied by prescribing a linearly increasing rotation, θ_Z^{RP3}, during a time-independent static step to achieve the desired imposed curvature at the beginning of relaxation process and the time-dependent response up to $1{\times}10^{10}$ s was computed. The same analysis was repeated for various imposed curvatures by varying the magnitude of the applied rotation θ_Z^{RP3}. The global curvature, κ is defined as,

$$\kappa = \frac{\theta_Z^{RP3}}{l} \tag{7}$$

where l is the length of the RVE.

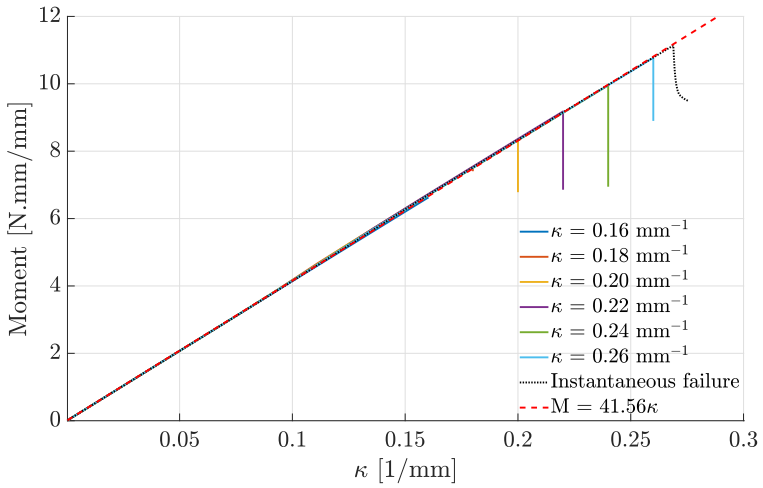

Fig. 3 Moment-curvature response of micromechanics model with $\phi_0 = 1^\circ$ and for different imposed curvatures.

In order to validate the model under static behavior, the mean stiffness of the linear response was calculated for this model as 41.56 N/mm using linear regression. Based on classical lamination theory, using the material properties given in Table 3 the corresponding stiffness for this laminate is 41.83 N/mm. Hence our model is in excellent agreement with the theoretical static response with an error of 0.7%.

The instantaneous failure curvature for this model was calculated as 0.27 mm^{-1} from the curve labeled as instantaneous failure in the Fig. 3. For this case, the analysis was terminated as the model failed to converge due to the

fiber microbuckling instability. The vertical drops of the moments in the curves with solid lines, obtained for different imposed curvatures and shown in Fig. 3 due to the stress relaxation behavior at the constant imposed curvature.

The typical resultant moment response with time during relaxation for different imposed curvatures are shown in Fig. 4. The gradual decrease of the moment with time corresponds to the relaxation behavior and the larger drop corresponds to rupture caused by fiber microbuckling and/or fiber-matrix debonding. The results show a clear negative correlation between increasing imposed curvature and the time taken for rupture. Even though we can identify rupture by the large drop in the moment response, the exact time for failure is not trivial to estimate. The observation of deformation growth aids the further understanding of the failure event.

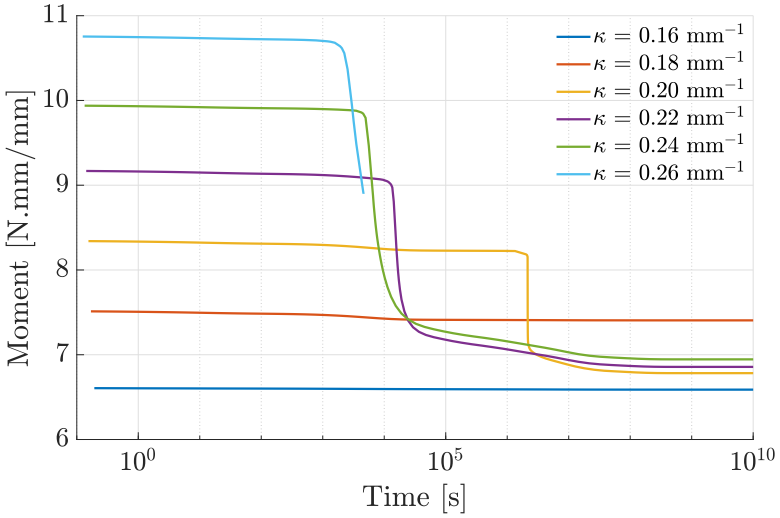

Fig. 4 Moment response with time of micromechanics model with ϕ_0 = 1° and for different imposed curvatures.

The deformation of the topmost fiber on the compression side was extracted from the simulation. The maximum slope at the center was calculated by taking numerical derivatives of the longitudinal fiber profile at each time frame. The maximum slope corresponds to the fiber misalignment angle at each time frame. Hence, the deformation growth was characterized as the growth of fiber misalignment angle, ϕ(t), during relaxation. Fig. 5 shows the evolution of the fiber misalignment angle over time for different imposed curvatures.

The sudden spike of the misalignment angle, ϕ, coincides with the large drop we observed in the moment response. So it is clear that fiber microbuckling is causing the failure of the laminate. The laminate does not show any time-dependent failure for low imposed curvatures of 0.16 and 0.18 mm^{-1}. All other cases where the imposed curvature is greater or equal than 0.2 mm^{-1} show a sudden spike of the misalignment angle. The spike in the misalignment angle happens over a longer time span for higher imposed curvature than for lower curvatures. Therefore, determining the exact time of the rupture could be rather subjective in these cases.

In order to maintain consistency, the time at which the growth rate of the fiber misalignment angle reaches its peak was defined as the rupture time. The growth rate was calculated as,

$$\text{Growth rate} = \frac{\Delta\phi}{\Delta(log_{10}t)} \tag{8}$$

where, ϕ is the misalignment angle and t is the time. Numerical differentiation was used to calculate the growth rate. Note that, here we are defining the growth rate as the change in log time. This allows us to scale up the time-dependent microbuckling event to determine the time taken for rupture. The growth rate of the fiber misalignment angle over time derived from the same set of simulations are shown in Fig. 6

In summary, for low imposed curvature (0.16 and 0.18 mm^{-1}) cases the deformation growth is gradual and remains bounded. The growth rate for these cases is slow and does not have any peaks. For higher imposed curvatures, closer to the laminates instantaneous failure curvature, the corresponding growth rate has a distinct peak and the deformation growth is unbounded and results in rupture due to fiber microbuckling.

In the next section, a similar analysis is carried out to investigate the influence of the initial misalignment angle of the fibers on the compression side.

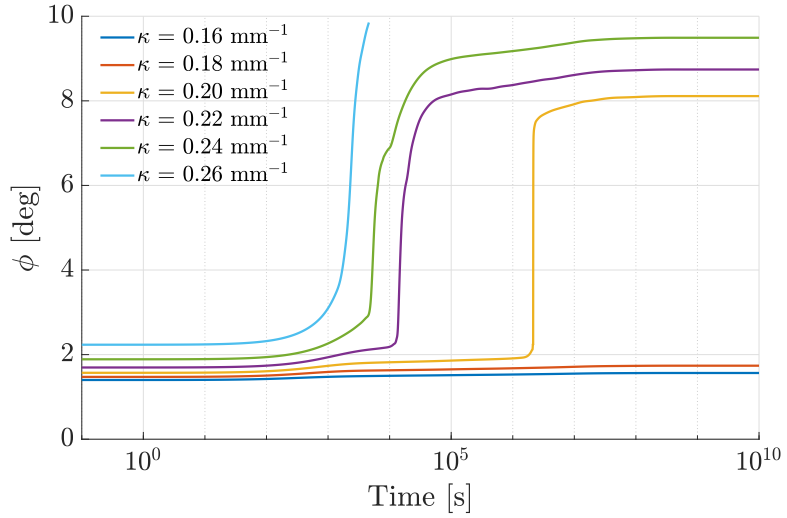

Fig. 5 Deformation growth is characterized as the growth of misalignment angle ϕ(t) with time for ϕ_0 = 1°and all imposed curvatures.

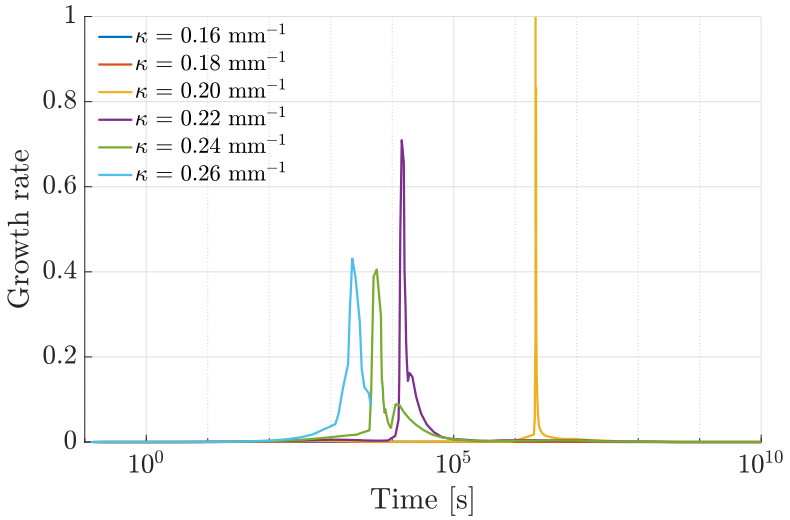

Fig. 6 Growth rate of misalignment angle ϕ(t) with time for ϕ_0 = 1° and all imposed curvatures.

IV. Influence of the initial misalignment angle

A parametric study was carried out to investigate the effect of varying the magnitude of the initial misalignment angle on the deformation growth and the time to rupture. Initial misalignment angles considered for this study were, ϕ_0 = {1°, 3°, and 5°}. All other geometric parameters such as fiber volume fraction and amplitude (λt) of the misalignment were kept constant. For each value of the initial fiber misalignment, a new RVE was created with the required geometry as explained in Section.II. All the other details of the micromechanics model and analysis were the same for all the models used for the parametric study.

The same analysis described in Section.III was carried out for each case. By applying a large imposed curvature the instantaneous failure curvature was determined as the upper bound for the imposed curvature during relaxation. Instantaneous failure curvatures corresponding to the cases ϕ_0 = 1°, 3°, and 5° are 0.270 mm^{-1}, 0.201 mm^{-1}, and 0.178 mm^{-1} respectively. The linear stiffness of the micromechanics model was also calculated using linear regression and the variation (less than 1%) between the models with different initial fiber misalignment angles is negligible.

Following the same procedure as the previous section, the relevant plots were obtained for comparison. The moment

resultant and the corresponding misalignment growth and growth rate over time for different initial misalignment angles are shown in Fig. 7. For each case, we vary the constant curvature imposed at the beginning of the relaxation process, with the instantaneous failure curvature as an upper bound, and decrease the magnitude until no failure occurred within $1{\times}10^{10}$ s. From the plots in Fig. 7, we can see that the range of imposed curvature where the rupture occurs within $1{\times}10^{10}$ s decreases with increasing initial misalignment angles. The instability event during the rupture spans over a longer period for larger initial misalignment angles compared to the $\phi_0 = 1°$ case.

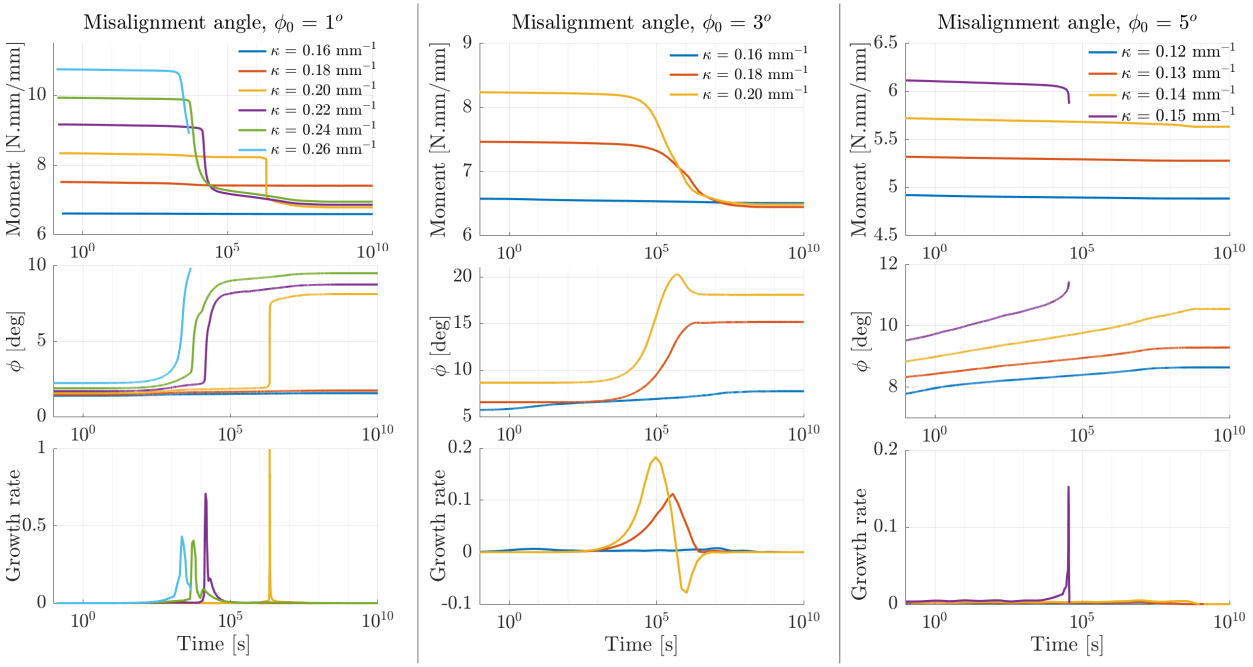

Fig. 7 Response of the moment resultant and corresponding misalignment growth and the rate of growth with time for the micromechanics model with $\phi_0 = 1°, 3°$, and $5°$ for different imposed curvatures.

The time to rupture was determined for all cases using the peak growth rate definition and its values have been plotted against the imposed curvatures in Fig. 8. The initial misalignment angle affects the time to rupture by order of magnitudes for the same imposed curvature. The left-most data point of each curve corresponds to the instantaneous failure curvature of the laminate. These results clearly show that the initial misalignment angle has a strong influence on the time to rupture. Even though the global trend is clear from Fig. 8, there is a need for more data points for intermediate values of imposed curvatures to obtain more detailed trends.

Further expansion of this parametric study can include relevant geometric parameters such as fiber volume fraction, amplitude of the misalignment, and different type of misalignment geometry. The scope of the present paper is limited to a misalignment defined as the arctan function described in Fig. 1.

V. Conclusions and Work in Progress

In this paper, a micromechanics-based finite element model for the long-term relaxation of thin laminates subjected to high bending curvatures has been proposed. Time-dependent deformation growth of the microstructure and the dominant failure mechanisms, fiber microbuckling and fiber-matrix interface debonding, induced during the stowage of high strain composite laminates have been included in the model. This study has provided valuable insight into the viscoelastic relaxation and failure mechanisms of high strain composites. The developed micromechanics model captured the deformation growth of the microstructure and the global resultant moment response well. The time to rupture due to fiber microbuckling was consistently determined for all the cases by calculating the peak growth rate of the misalignment angle. The presented parametric analysis of the initial misalignment angle shed insights into the global trend of deformation growth and eventual rupture due to fiber microbuckling. Further expansion into relevant

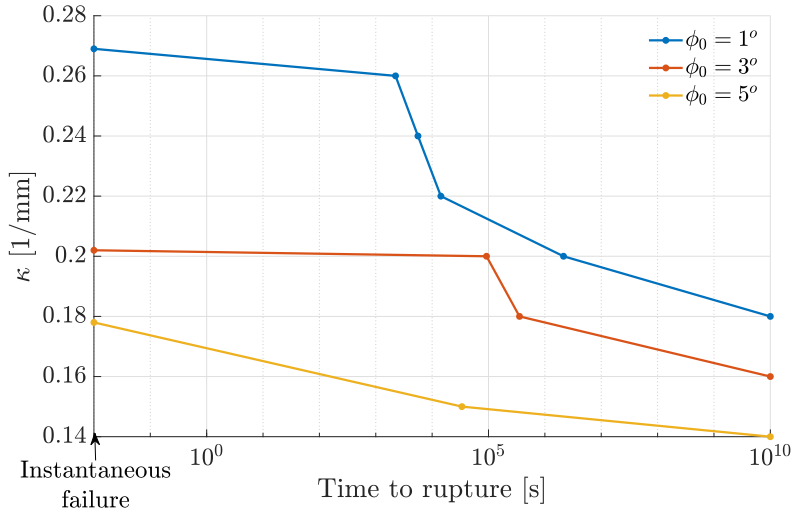

Fig. 8 Time for rupture of RVEs with different initial misalignment angles.

geometric parameters such as fiber volume fraction and various types of misalignment will help us understand the influence of the fiber microbuckling failure mechanism. Results from the expansion of these parametric studies will be presented in future publications.

Acknowledgments

The authors acknowledge financial support from the Space Solar Power Project at Caltech. Test materials for this study were provided by Nick Patz (Patz Materials & Technology).

References

[1] Schapery, R., "Nonlinear viscoelastic solids," *International Journal of Solids and Structures*, Vol. 37, 2000, pp. 359–366.

[2] Murphey, T. W., Francis, W., Davis, B., and Mejia-Ariza, J. M., "High strain composites," *2nd AIAA spacecraft structures conference*, 2015, p. 0942.

[3] Li, J., Kwok, K., and Pellegrino, S., "Large-strain thermoviscoelastic model of StratoFilm," *Mechanics of Time-Dependent Materials*, 2016.

[4] Rose, T. J., Medina, K., Francis, W., Kwok, K., Bergan, A., and Fernandez, J. M., "Viscoelastic Behavior of High Strain Composites," *AIAA/ASME/ASCE/AHS/ASC High-Strain Composite Materials and Structures II*, 2019.

[5] Ubamanyu, K., Ghedalia, D., Hasanyan, A. D., and Pellegrino, S., "Experimental Study of Time-dependent Failure of High Strain Composites," *AIAA Scitech 2020 Forum*, 2020, p. 0207.

[6] Medina, K., Rose, T., and Francis, W., "Long-term Stress Rupture Limitations of Unidirectionasl High Strain Composites in Bending," *Proceedings of the American Society for Composites—Thirty-third Technical Conference*, 2018.

[7] Vogler, T., Hsu, S.-Y., and Kyriakides, S., "On the initiation and growth of kink bands in fiber composites. Part II: analysis," *International Journal of Solids and Structures*, Vol. 38, No. 15, 2001, pp. 2653–2682.

[8] Budiansky, B., Fleck, N., and Amazigo, J., "On kink-band propagation in fiber composites," *Journal of the Mechanics and Physics of Solids*, Vol. 46, No. 9, 1998, pp. 1637–1653.

[9] Brinkmeyer, A., Pellegrino, S., and Weaver, P. M., "Effects of long-term stowage on the deployment of bistable tape springs," *Journal of Applied Mechanics*, Vol. 83, No. 1, 2016, p. 011008.

[10] Kwok, K., and Pellegrino, S., "Micromechanics models for viscoelastic plain-weave composite tape springs," *AIAA Journal*, Vol. 55, No. 1, 2017, pp. 309–321.

[11] Yapa Hamillage, M., Leung, C., and Kwok, K., "Viscoelastic modeling and characterization of thin-ply composite laminates," *Composite Structures*, Vol. 280, 2022, p. 114901. doi:https://doi.org/10.1016/j.compstruct.2021.114901.

[12] Sullivan, J., "Creep and physical aging of composites," *Composites Science and Technology*, Vol. 39, No. 3, 1990, pp. 207–232.

[13] Lopez Jimenez, F., "Numerical Modeling of Stress Concentration Around Failed Fibers in Unidirectional Composites," *AIAA Scitech 2021 Forum*, 2021, p. 0087.

[14] Borowski, E. C., Soliman, E. M., Khan, A. I., and Taha, M. M. R., "Stowage and Deployment of a Viscoelastic Orthotropic Carbon-Fiber Composite Tape Spring," *Journal of Spacecraft and Rockets*, Vol. 55, No. 4, 2018, pp. 829–840.

[15] "ABAQUS Analysis User's Manual," , 2019.

[16] Amacher, R., Cugnoni, J., Botsis, J., Sorensen, L., Smith, W., and Dransfeld, C., "Thin ply composites: Experimental characterization and modeling of size-effects," *Composites Science and Technology*, Vol. 101, 2014, pp. 121–132.